Research Article | Vol. 27, No. 13 | 24 Jun 2019 | OPTICS EXPRESS 17507
Optics EXPRESS

Tunable, dual wavelength and self-Q-switched Alexandrite laser using crystal birefringence control

GORONWY TAWY* AND MICHAEL J. DAMZEN

Photonics Group, The Blackett Laboratory, Dept. of Physics, Imperial College London, Prince Consort Road, London, SW7 2AZ, UK
*goronwy.tawy12@imperial.ac.uk

Abstract: We present a red-diode-pumped Alexandrite laser with continuous wavelength tunability, dual wavelength and self-Q-switching in an ultra-compact resonator containing only the gain medium. Wavelength tuning is obtained by varying the geometrical path length and birefringence by tilting a Brewster-cut Alexandrite crystal. Two crystals from independent suppliers are used to demonstrate and compare the performance. Wavelength tuning between 750 and 764 nm is demonstrated in the first crystal and between 747 and 768 nm in the second crystal. Stable dual wavelength operation is also obtained in both crystals with wavelength separation determined by the crystal free spectral range. Temperature tuning was also demonstrated to provide finer wavelength tuning at a rate of $-0.07\,\mathrm{nm\,K^{-1}}$. Over a narrow tuning range, stable self-Q-switching is observed with a pulse duration of 660 ns at 135 kHz, which we believe is the highest Q-switched pulse rate in Alexandrite to date. Theoretical modelling is performed showing good agreement with the wavelength tuning and dual wavelength results.

Published by The Optical Society under the terms of the Creative Commons Attribution 4.0 License. Further distribution of this work must maintain attribution to the author(s) and the published article's title, journal citation, and DOI.

1. Introduction

Wavelength tunable lasers emitting in the near-infrared attract interest due to several applications including remote sensing [1], quantum technologies [2] and biophotonics [3]. Dual wavelength lasers have a number of interesting applications such as coherent terahertz wave generation [4] and optical communications [5]. The solid-state laser material Alexandrite, or Chromium doped Chrysoberyl (Cr^{3+}:$BeAl_2O_4$), has tunability in this region (700-850 nm) [6, 7] and has gained new interest due to the development of red-diode lasers as efficient and low cost pump sources. Studies have demonstrated low cost and low threshold [8], high power [9], broad wavelength tuning and highly efficient [10, 11] red-diode-end-pumped continuous-wave (CW) Alexandrite lasers. High power side pumped [12] and vortex mode generation [13] has also been demonstrated in CW-operation. In pulsed operation, active, cavity dumped [14] and passive [15] Q-switched operation has been achieved. More recently single-longitudinal-mode operation has been achieved with red-diode pumping in both Q-switched and CW operation [16–18].

Alexandrite has a number of key advantages as a laser gain medium. Its high fracture resistance and good thermal conductivity (×5 and ×2 of Nd:YAG respectively) allow intense pumping without risk of crystal fracture [6]. Its broad absorption band across the visible region allows efficient direct pumping by commercially available red diodes (630-680 nm). This enables an affordable, compact and simple system to be realised as well as allowing high power scaling. Ground state absorption (GSA) at the laser wavelength and excited state absorption (ESA) at the pump and laser wavelengths play an important role in the efficiency and wavelength tuning range of Alexandrite [19]. Recent work in our group has shown the optimised requirements and demonstrated the highest slope efficiency (54 %) and largest tuning range (>100 nm) for a red-diode-pumped Alexandrite laser [11].

In prior work, wavelength tuning was usually accomplished with a birefringent filter in an

#363806 https://doi.org/10.1364/OE.27.017507
Journal © 2019 Received 4 Apr 2019; revised 14 May 2019; accepted 14 May 2019; published 10 Jun 2019

Optics EXPRESS

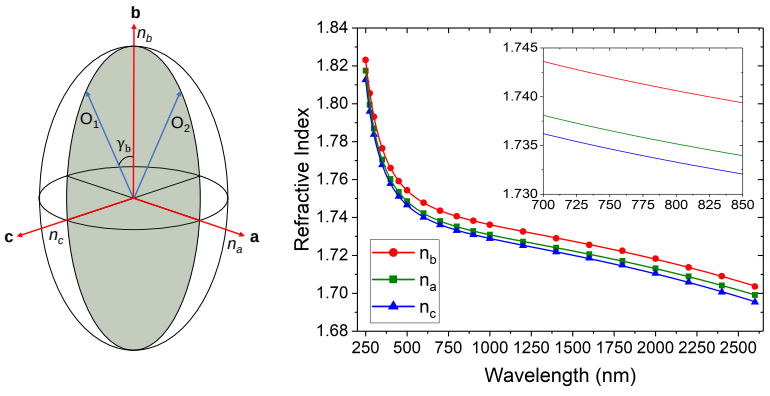
extended cavity with intra-cavity lenses or curved mirrors for TEM_{00} selection. Birefringent filters have also been used in generating dual wavelength operation in Alexandrite [20] and other laser gain media [21, 22]. Recent interest has been towards using off-axis birefringent filters which provide tunability in the dual wavelength separation [23, 24]. However, it is generally found that there is a significant loss of efficiency in extended cavities compared to compact cavities due to the insertion losses and the influence of thermal aberrations [25].

In this report wavelength tuning is obtained by using the birefringent properties of Alexandrite by tilting a Brewster-cut Alexandrite crystal inside a plane-plane cavity. This allows a short ultra-compact cavity to be built which provides excellent beam quality and high output power. Continuous tuning between 747 and 768 nm is demonstrated and is limited only by the free spectral range of the crystal. Stable dual wavelength operation is obtained with a wavelength separation of 12 nm. Fine tuning of the wavelength at a rate of $-0.07\,\mathrm{nm\,K^{-1}}$ is also achieved by varying the crystal temperature. Stable self-Q-switching is observed over a narrow tuning range with 660 ns pulse duration at a repetition rate of 135 kHz - the highest Q-switched pulse rate to date for Alexandrite. This realises further potential for this system as an ultra-compact, high repetition-rate source.

2. Birefringent properties of Alexandrite

The Chrysoberyl host in Alexandrite is orthorhombic with low crystal symmetry. It is therefore optically biaxial with the principal plane of the dielectric constants along the crystal axes with refractive indices: $n_b > n_a > n_c$ [6]. Its birefringent properties have been well described in [26], however a brief overview will be stated for sake of completeness. The two optic axes, O_1 and O_2, lie in the bc-plane at an angle $\pm\gamma_b$ to the b-axis, as illustrated in Fig. 1(a). The angle, γ_b, depends on all three refractive indices [27]:

$$\sin\gamma_b = \frac{n_b}{n_a}\sqrt{\frac{n_a^2 - n_c^2}{n_b^2 - n_c^2}}. \tag{1}$$



(a) (b)

Fig. 1. (a) Index ellipsoid of Alexandrite. Optic axes, O_1 and O_2, lie in the bc-plane (shown shaded). (b) Refractive index for light polarised to the a, b and c crystal axes as a function of wavelength. Inset shows refractive index in the lasing band of Alexandrite between 700 nm and 850 nm. Data taken from [6] with Sellmeier fit applied.

Figure 1(b) shows the dispersion of the principal refractive indices at room temperature. A Sellmeier fit is applied to the data to determine the refractive indices across the lasing region of

Optics EXPRESS

Alexandrite. Table 1 shows the refractive index at 700, 750 and 800 nm as well as the difference between the principal refractive indices. Substituting the values from this table into Eq. (1) gives $\gamma_b = 30.3°$ at 700 nm increasing to 30.5° at 800 nm. Therefore the dispersion of γ_b is relatively weak over the lasing region of Alexandrite. In this work the refractive indices and difference between the refractive indices at 750 nm will be used, this gives $\gamma_b = 30.4°$.

Table 1. Refractive index along the a, b and c crystal axes and refractive index difference at 700, 750 and 800 nm determined from Sellmeier fit in Fig. 1(b).

Wavelength (nm)	n_a	n_b	n_c	$n_b - n_a$	$n_a - n_c$	$n_b - n_c$
700	1.7381	1.7436	1.7362	0.0055	0.0018	0.0074
750	1.7365	1.7420	1.7347	0.0055	0.0018	0.0074
800	1.7352	1.7406	1.7333	0.0055	0.0018	0.0073

For a beam travelling through an Alexandrite crystal at an arbitrary angle there are two refractive indices associated to two orthogonal polarisation states. The phase difference between the two states is given by

$$\Delta\phi = \frac{2\pi}{\lambda}\Delta nL \tag{2}$$

where λ is the wavelength, L is the mean geometrical path travelled in the crystal and Δn is the difference between the refractive indices of the two polarisations. The condition for low-loss of the crystal in the laser cavity is for its birefringence to act as a full waveplate, i.e. $\Delta\phi = 2\pi m$, where m is an integer, therefore the wavelengths at low loss transmission are

$$\lambda_m = \frac{\Delta nL}{m}. \tag{3}$$

The separation between adjacent wavelength orders ($\Delta m = 1$) is the free spectral range (FSR), $\Delta\lambda_{\mathrm{FSR}}$, which is approximately given by

$$\Delta\lambda_{\mathrm{FSR}} = \lambda_m - \lambda_{m-1} \approx \frac{\lambda_m^2}{\Delta nL} \tag{4}$$

Changing L and Δn by tilting the crystal in a fixed laser cavity provides wavelength tunability if the order m is unchanged (Eq. (3)). There is also the possibility of two wavelengths accessing equal gain leading to dual wavelength at the FSR separation. To study these effects a plane-plane cavity with a Brewster-cut Alexandrite crystal was built as described in Section 3.

3. Alexandrite compact laser cavity with crystal birefringent tuning

3.1. Compact cavity

Figure 2 shows an Alexandrite laser resonator formed of a Brewster-cut Alexandrite crystal, dichroic back mirror (BM) that was highly transmissive at the pump wavelength (~ 635 nm) and highly reflective at the laser wavelength (700-820 nm) and an output coupler (OC). Two commercially available Brewster-cut Alexandrite crystals from different suppliers were used in the experiment to check consistency. Crystal 1 was a Brewster-cut rod with 4 mm diameter and 0.22 at.% Cr-doping. Crystal 2 was a Brewster-cut slab with 4×4 mm cross section and 0.24 at.% Cr-doping. Both had a nominal length of $L_C = 8.0$ mm (perpendicular end-face separation

Optics EXPRESS

of L_0 = 6.9 mm). The optical path length of the cavity mode was ~ 24 mm. The temperature of crystal 1 was set to 50 °C to optimise its performance [19] whereas crystal 2 had to be initially set at 16 °C as it shared the same chiller as the pump. The reflectivities of the output couplers used were R_{OC1} = 99.0 % and R_{OC2} = 99.5 % for the cavities containing crystals 1 and 2, respectively. Cavity stability was ensured with the positive pump-induced thermal lens in the laser crystal.

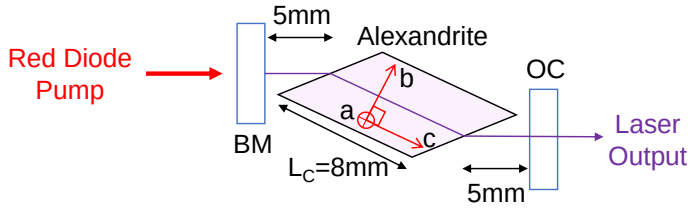


Fig. 2. Alexandrite compact laser cavity with crystal axes shown.

The Alexandrite crystal was end-pumped through the back mirror by a fibre coupled diode module. The diode delivery fibre had a core diameter of 105 µm and NA = 0.22. The fibre output was collimated with a 35 mm lens and focused with an aspheric lens of focal length, f = 50 mm, producing a focal waist radius ~ 75 µm on the Alexandrite end-face. The pump beam quality was measured to be M^2 ~ 50. At maximum drive current the output power of the module was 5.5 W. The central wavelength and linewidth at maximum pump power were measured to be 637 nm and 1.2 nm, respectively. The polarisation of the pump fibre output was partially scrambled with ~ 70 % of the power in its major axis. A half waveplate was used to rotate the major axis to the crystal b-axis. Approximately 75 % of the pump was absorbed by the crystal.

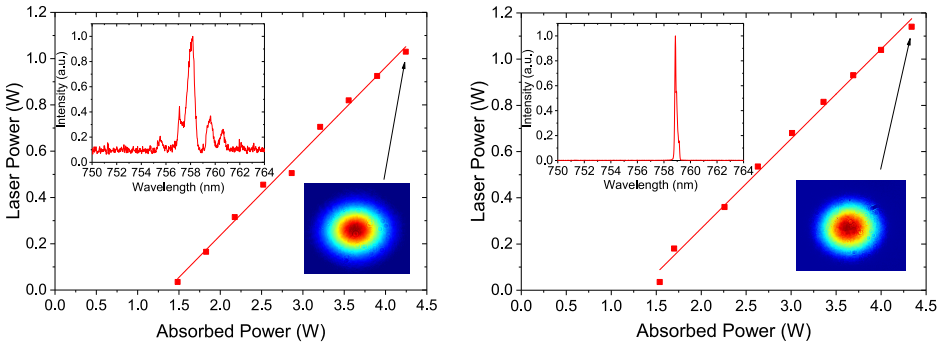


Fig. 3. Laser power as a function of absorbed pump power with linear fit. Inset shows laser wavelength spectrum and beam profile at maximum power for (a) crystal 1 and (b) crystal 2.

Figures 3(a) and 3(b) show the laser power as a function of the absorbed power for crystal 1 and 2, respectively. For crystal 1, at maximum pump power the output power was 1.03 W. The threshold and slope efficiency were 1.3 W and 36 %, respectively. The beam quality was measured to be M^2 = 1.1 in both directions though the beam was slightly elliptical due to the astigmatism caused by the Brewster cut crystal (see inset of Fig. 3(a)). The spectrum had a main peak at ~ 758 nm with additional smaller peaks separated by around 1-1.5 nm with an overall spectral width of ~ 5 nm.

Crystal 2 performed marginally better achieving an output power of 1.14 W. The threshold

Optics EXPRESS

and slope efficiency were 1.5 W and 39 %, respectively. The output spatial mode was similar to that of crystal 1 with M^2 = 1.1. The laser operated at a wavelength of 758.9 nm with a single peak with spectral width limited by the resolving power of the spectrometer (~ 0.2 nm).

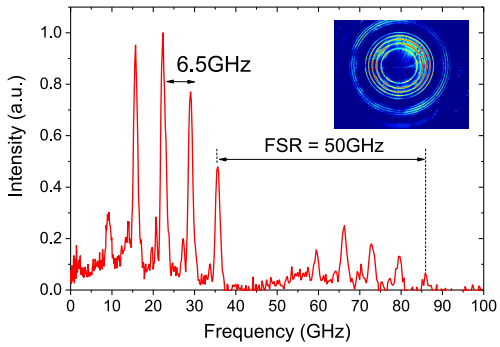


Fig. 4. Frequency spectrum for crystal 2 with Fabry-Perot interference pattern shown in inset.

To achieve better resolution, the laser frequency spectrum was measured using a free space Fabry-Perot etalon with a FSR of 50 ± 4 GHz (where the uncertainty is due to a ±0.25 mm uncertainty in the etalon mirror separation). Figure 4 shows the frequency spectrum of the laser with crystal 2. The laser operated on 4-5 longitudinal modes with an overall linewidth of ~ 15 GHz. The measured mode spacing of 6.5 ± 0.5 GHz is consistent with the theoretical mode spacing of 6.3 ± 0.5 GHz based on the experimental cavity optical path length of 24 ± 2 mm (see Fig. 2).

3.2. *Birefringent wavelength tuning with Alexandrite crystal*

Birefringent wavelength tuning was obtained by tilting the Brewster-cut Alexandrite crystal. Figures 5 (a) and 5 (b) shows two views of the beam path through the Alexandrite crystal and the parameters used to define the crystal tilt.

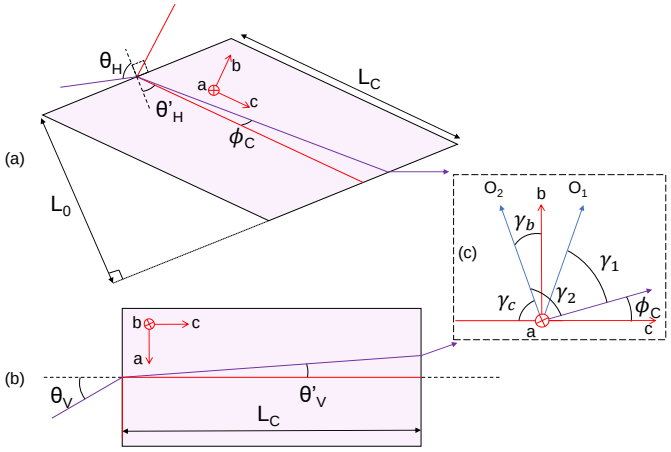


Fig. 5. (a) Top-view showing beam propagation in the crystal bc-plane. (b) Side-view showing beam propagation in the crystal ac-plane. (c) Angular position of the optic axes (O_1, O_2) with respect to the crystal b and c axes (γ_b,γ_c) and to the beam path (γ_1,γ_2).

The manufactured crystals in this work were specified as c-cut with Brewster-angled end faces.

Optics EXPRESS

When the input beam was incident at a horizontal angle of incidence (θ_H) equal to the Brewster angle ($\theta_B \approx \tan^{-1} n_b \approx 60.1°$), the beam path should be along the crystal c-axis. Manufacturing tolerances meant there is likely to be some small uncertainty in this path, and will be discussed later.

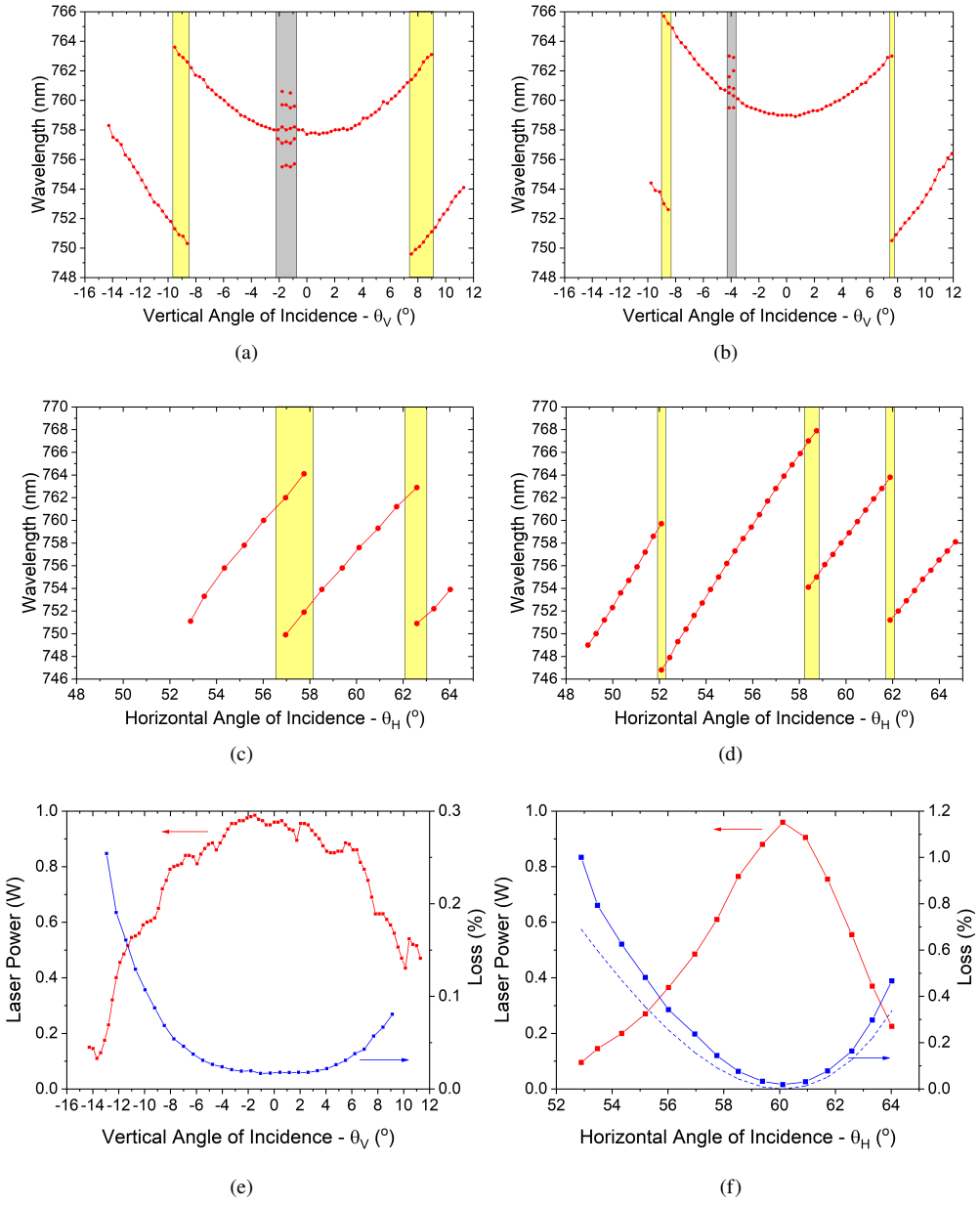


Fig. 6. Wavelength as a function of vertical angle of incidence for (a) crystal 1 and (b) crystal 2, and as a function of horizontal angle of incidence for (c) crystal 1 and (d) crystal 2. Yellow region indicates dual wavelength operation with ~ 12 nm separation. Grey region is where spectrum was highly modulated. Laser power and single surface loss for crystal 1 as a function of (e) vertical angle of incidence and (f) horizontal angle of incidence with theoretical Fresnel loss shown as dashed line.

Optics EXPRESS

To study wavelength tuning, the crystal was tilted in two ways. In one case, the angle of incidence in the vertical plane (crystal ac-plane) was changed, as shown schematically in Fig. 5(b). The crystal is tilted such that the beam is incident at a vertical angle of incidence, θ_V, with respect to the surface normal, and is refracted at an angle θ'_V with respect to the nominal direction of the crystal c-axis, with the horizontal angle of incidence fixed at $\theta_H = \theta_B \approx \tan^{-1} n_b \approx 60.1°$. The second case was to change the horizontal angle of incidence, θ_H from its Brewster angle case, θ_B, providing an internal horizontal angle $\phi_C = \theta'_H - \theta'_B$ with respect to the crystal c-axis and with the vertical angle of incidence fixed at $\theta_V = 0°$, as shown in Fig. 5(a).

Figures 6(a) and 6(b) show the laser wavelength as a function of the vertical angle of incidence (θ_V) with the horizontal angle of incidence fixed ($\theta_H = \theta_B$) for crystals 1 and 2, respectively. The corresponding laser power and measured surface reflection loss for crystal 1 are shown in Fig. 6(e). At $\theta_V = 0°$ the laser wavelength is at $\sim$ 758 nm and $\sim$ 759 nm for crystal 1 and 2, respectively. Changing the vertical angle of incidence (θ_V) either in the positive or negative direction increases the laser wavelength approximately quadratically with the laser power > 0.8 W up to $\theta_V = \pm 6°$.

At a vertical angle of incidence, $\theta_V \approx \pm 8 - 9°$, dual wavelength operation with a FSR separation of $\sim$ 12 nm and $\sim$ 13 nm for crystal 1 and 2, respectively was observed with the laser power at $\sim$ 0.6 W. This will be discussed in greater detail later. Reducing/increasing the vertical angle of incidence (θ_V) beyond the region of dual wavelength operation increased the wavelength further but from the shorter wavelength. The laser linewidth was measured across the tuning range and was found to be $\sim$ 15 GHz and in dual wavelength operation each wavelength also had a similar linewidth.

For both crystal 1 and 2 there was a region over which the linewidth broadened and the spectrum became modulated (peaks of modulation shown in Figs. 6(a) and 6(b)). This region also corresponded to the position of the highest laser power. We believe that this region corresponds to the beam travelling along the c-axis where the weak birefringence gives poor wavelength discrimination and the good matching of the polarisation to the higher gain b-axis gives higher output power. The asymmetric location of the modulated region at $\theta_V \sim -1°$ and $\theta_V \sim -4°$ for crystal 1 and 2, respectively is believed to be due to a manufacturing angular misalignment between the Brewster-cut and the crystal c-axis. Temporal measurements of the laser output for crystal 2 lasing in this $\theta_V \sim -4°$ region showed stable self-Q-switching; this is discussed in greater detail in section 3.4.

Figures 6(c) and 6(d) shows the wavelength as a function of the horizontal angle of incidence (θ_H) with $\theta_V = 0°$ for both crystals. The laser power and surface loss for crystal 1 is shown in Fig. 6(f). At $\theta_H = \theta_B$, crystal 1 operated at a wavelength of $\lambda = 757.6$ nm with the laser power at 0.96 W. When increasing the horizontal angle of incidence the wavelength increased approximately linearly until dual wavelength operation was observed with a separation of $\sim$ 12 nm at $\theta_H \approx 62°$. At this angle of incidence the output power was 0.56 W due to the increased Fresnel loss from the crystal surface (see Fig. 6(f)). Similar results were observed in crystal 2.

Broader tuning was obtained when decreasing the horizontal angle of incidence, with tuning over 750-764 nm obtained twice for crystal 1. Stable dual wavelength operation with 12 nm separation was obtained at around $\theta_H = 57 - 58°$ at an output power of around 0.5 W. Tuning was maintained until the cavity losses exceeded the gain at $\theta_H \sim 52°$. With crystal 2, broad tuning between 747 and 768 nm was obtained. Stable dual wavelength operation at 0.8-0.9 W was obtained at $\theta_H = 58 - 59°$ with a FSR separation of $\sim$ 13 nm.

As indicated in Figs. 6(a)-6(d) several regions of dual wavelength operation were observed for crystal 1 and 2 for either horizontal or vertical tilting. Figure 7 shows an example of a dual wavelength spectrum for crystal 1 at $\theta_V = 8.3°$ and $\theta_H = \theta_B$. The onset of dual wavelength operation can be explained by considering the gain and loss conditions. Under optimal conditions the laser operates at a wavelength determined by the laser gain (which is temperature dependent),

Optics EXPRESS

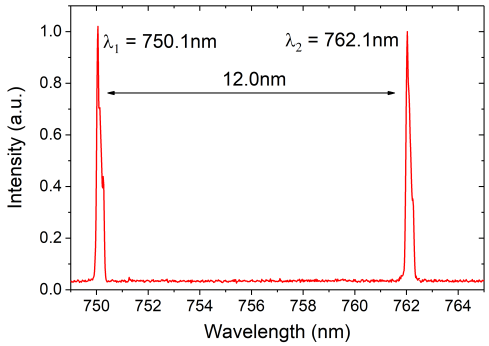


Fig. 7. Laser spectrum for crystal 1 at $\theta_V = 8.3°$ and $\theta_H = \theta_B$ where dual wavelength operation was observed at wavelengths of 750.1 nm and 762.1 nm (12 nm separation).

cavity losses and birefringent filtering transmission (Eq. (3)). The filtering transmission are separated by the FSR, therefore single wavelength operation occurs at regions where the overall gain is higher at that wavelength than at the next wavelengths located at $\pm\lambda_m^2/\Delta nL$. Dual wavelength operation occurs when the filtering transmission has been shifted such that the two low loss transmission (λ_m and λ_{m-1} or λ_m and λ_{m+1}) occupy two regions of equal gain, typically equidistant from the optimal wavelength. This is evident in the experimental results where dual wavelength operation is typically at 750 and 764 nm and the optimal wavelength is at 758 nm. The broad wavelength tuning in Fig. 6(d) is an exception to this and may be due to the overall gain profile also shifting due to the wavelength dependence of the reflectivity of the output coupler. The differences between the measured FSR separation for crystal 1 and 2 could be attributed to slightly different length of each crystal.

3.3. *Temperature tuning*

The temperature dependence of the wavelength was also investigated for both crystals at Brewster angle incidence ($\theta_V = 0°$ and $\theta_H = \theta_B$) by varying the water temperature of the crystal at maximum pump power.

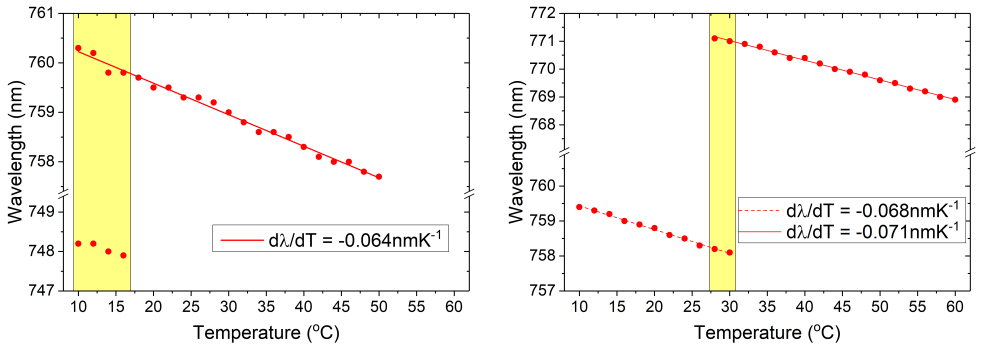


Fig. 8. Wavelength as a function of water temperature for (a) crystal 1 (b) crystal 2 with yellow region indicating dual wavelength operation.

Figre 8 shows the wavelength as a function of the water temperature for both crystals. Temperature variation enabled fine wavelength tuning at a rate ~ -0.07 nm K^{-1}. Dual wavelength

Optics EXPRESS

operation was obtained at low temperatures for crystal 1 and at mid temperatures for crystal 2. This difference could again be attributed to the slightly different length of each crystal as well as different misalignment of the crystal c-axis relative to the Brewster-cut.

3.4. Self-Q-switching

The results presented so far have demonstrated a tunable laser and regions of dual wavelength laser operation with good spatial quality and narrow linewidth using an ultra-compact cavity. The broad and modulated spectrum observed in both crystals disrupted narrow line tunability but only over a narrow tilt angular region and with no change in the central wavelength. Temporal measurements with crystal 2 showed that the laser was self-Q-switching (SQS) in this region.

In order to fully assess the performance of the SQS laser the cavity was re-optimised. The cavity was shortened from an optical path length of 24 mm to 20 mm to optimise the output power. The water temperature of the crystal was varied between 10 °C and 60 °C to analyse the temperature dependence of the Q-switched pulses. It was found that stable Q-switching only occurred between 10 °C and 20 °C. Furthermore, contrary to the standard expectation of Alexandrite [11], the average laser power was found to increase with decreasing temperature (with little change in wavelength) over the region 20-10 °C where stable SQS occurred - this discrepancy requires a detailed assessment of the Q-switching loss mechanism which is discussed later. The maximum laser power was at a water temperature of 10 °C. Figure 9(a) shows the laser power as a function of the absorbed power at this temperature.

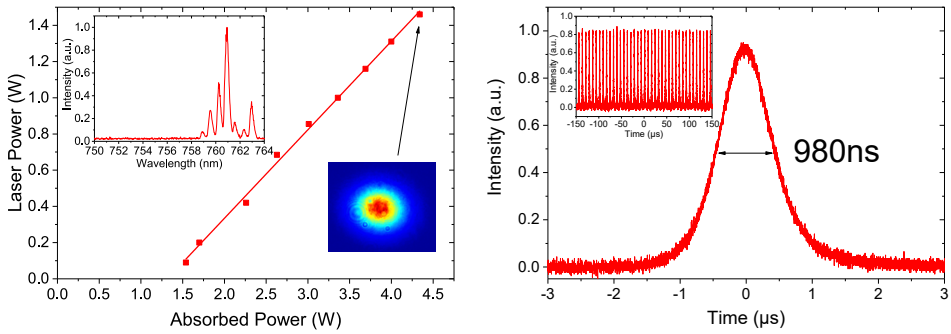


Fig. 9. (a) Average laser power as a function of absorbed power for SQS laser. Inset shows modulated spectrum and spatial beam profile at maximum power. (b) Temporal output showing 980 ns Q-switched pulse at 1.46 W of average power. Inset shows long-capture of stable Q-switched pulse train.

The laser operated at a maximum average power of 1.46 W and a slope efficiency of 49 %. The beam quality was measured to be $M^2 \leq 1.2$ and the output mode unchanged compared to that observed when operating in CW. The pulse duration was 980 ns at a repetition rate of 135 kHz. The inset in Fig. 9(b) shows a long capture of the pulse train demonstrating the stability of the system. The cavity was optimised further to minimise the pulse duration. At a water temperature of 16 °C and maximum pump power a pulse duration of 660 ns at 135 kHz was achieved with the average laser power at 1.32 W. This pulse duration is believed to be the shortest for any SQS Alexandrite laser. The pulse energy and peak power were 9.6 μJ and 14.6 W, respectively with a 4 % standard deviation in the pulse energy. SQS operation was non-critical with the same standard deviation in pulse energy measured with variations of ±1 mm in the pump focus and ±1° in the vertical angle of incidence, θ_V.

Optics EXPRESS

SQS in Alexandrite has been previously reported [8,10,28,29]. The pump wavelength has been attributed as a key parameter, with shorter pump wavelengths giving rise to a greater likelihood of SQS [29]. Despite this, recent results with short wavelength green pumping has reported no observations of SQS when operating in CW and mode-locked regimes [30–34]. A more likely cause that has been discussed in other Cr-doped gain media is a population-induced variation in the refractive index [35,36]. The coupling of the Cr-ions in the crystal field changes depending on whether or not they are excited. This induces a so called "population lens" which depends on the population inversion density [35]. A "fast" loss variation in the population inversion as opposed to a "slow" response induced by a thermal lens seems as a more plausible cause for the pulse duration and repetition rates measured in this experiment. There is limited work on measuring the population lens in the case of Alexandrite, however the underlying mechanism of a non-zero polarisability difference has been measured [37]. Accurate measurement of the population lens is in progress for future work.

4. Theoretical model of wavelength tuning

The wavelength tuning can be modelled on the geometry of the crystal and its birefringence. This provides validity of the basic mechanisms underlying the experiment as well as providing equations that allow an understanding of the key parameters that can be more generally controlled to give the required tunability or dual wavelength separation. In a Brewster-cut crystal, for a general beam path with internal angles θ'_H and θ'_V, in orthogonal horizontal and vertical directions, the geometrical path length is given by

$$L = \frac{L_0}{\cos\theta'_H \cos\theta'_V}, \tag{5}$$

where L_0 is the perpendicular distance between the end-face two surfaces (see Fig. 5(a)). The refractive index difference for a general beam path in a biaxial crystal is [27]

$$\Delta n = (n_b - n_c)\sin\gamma_1 \sin\gamma_2 = \Delta n_{bc} \sin\gamma_1 \sin\gamma_2, \tag{6}$$

where γ_1, γ_2 are the angles between the beam propagation and the optic axes O_1, O_2 (see Fig. 5(c)). Substituting these expressions into Eq. (3) gives

$$\lambda_m = \frac{\Delta n_{bc} L_0}{m} \frac{\sin\gamma_1 \sin\gamma_2}{\cos\theta'_H \cos\theta'_V}. \tag{7}$$

For a perfect Brewster-cut crystal the minimum reflection loss is at $\theta'_V = 0°$ and $\theta'_H = \theta'_B$. Under these conditions in the ideal case the beam travels along the c-axis of the crystal ($\phi_C = 0°$), therefore $\gamma_1 = \gamma_c$ and $\gamma_2 = \gamma_b + \pi/2$. Using Eq. (7) the wavelength under these conditions, λ_{m_0}, is given by

$$\lambda_{m_0} = \frac{\Delta n_{bc} L_0}{m} \frac{\cos^2\gamma_b}{\cos\theta'_B}. \tag{8}$$

Assuming the order m is unchanged then Eq. (7) and (8) can be combined to derive an expression for λ at any internal angle (θ'_H, θ'_V) given λ_{m_0}

$$\lambda_m\left(\theta'_H, \theta'_V\right) = \lambda_{m_0}\left(\frac{\cos\theta'_B}{\cos\theta'_H \cos\theta'_V}\right)\left(\frac{\sin\gamma_1 \sin\gamma_2}{\cos^2\gamma_b}\right). \tag{9}$$

In Eq. (9) the first bracketed term represents the fractional change in wavelength due to the change in the geometrical path length inside the crystal. The second term, which depends on the angle between the beam and the optic axes represents the fractional change in the refractive

Optics EXPRESS

index difference. The equation can be easily adapted to represent the wavelength in terms of changes to the vertical angle of incidence (θ_V) and separately the horizontal angle of incidence (θ_H). When changing the vertical angle of incidence (θ_V) with $\theta_H = \theta_B$, γ_1 and γ_2 are related to θ'_V according to $\cos\gamma_1 = \cos\theta'_V \cos\gamma_c$ and $\cos\gamma_2 = \cos\theta'_V \cos(\gamma_b + \pi/2)$. Equation (9) can then be simplified to

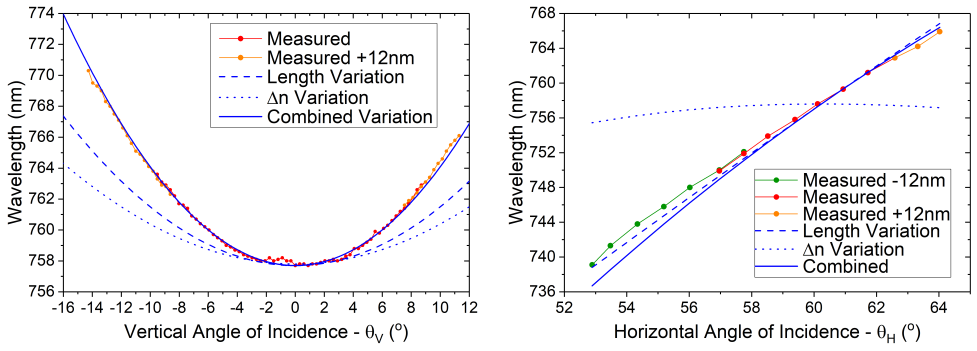
$$\lambda_m\left(\theta'_V\right) = \lambda_{m_0}\left(\frac{1}{\cos\theta'_V}\right)\left(\frac{1-\cos^2\theta'_V\cos^2\gamma_c}{\cos^2\gamma_b}\right). \tag{10}$$

A similar expression can be obtained for the case of tuning with changing the horizontal angle of incidence (θ_H) with $\theta_V = 0°$. The expression for γ_1 and γ_2 are simpler: $\gamma_1 = \gamma_c - \phi_c$ and $\gamma_2 = \gamma_b + \pi/2 - \phi_c$. Substituting these into Eq. (9) and simplifying gives

$$\lambda_m\left(\theta'_H\right) = \lambda_{m_0}\left(\frac{\cos\theta'_B}{\cos\theta'_H}\right)\left(\frac{\cos(\gamma_b+\phi_c)\cos(\gamma_b-\phi_c)}{\cos^2\gamma_b}\right). \tag{11}$$

4.1. Wavelength tuning: comparing model with experiment

Equations (10) and (11) can be compared to the experimental wavelength tuning of Figs. 6(a) and 6(c). Figure 10(a) shows the measured wavelength as a function of the vertical angle of incidence (θ_V) with the order m of Fig. 6(a) unchanged and with the order $m+1$ shifted by +12 nm. The theoretical wavelength given by Eq. (10) shows how the wavelength changes according to the change in path length (dashed curve), refractive index (dotted curve) and the combined change (solid curve). The results are in excellent agreement with the theoretical model when accounting for the combined change in path length and change in refractive index.



(a) (b)

Fig. 10. (a) Measured and theoretical wavelength (blue) as a function of the vertical angle of incidence with $m+1$ order shifted +12 nm. (b) Measured and theoretical wavelength (blue) as a function of the horizontal angle of incidence with $m+1$ order shifted +12 nm and $m-1$ order shifted −12 nm.

Figure 10(b) shows the wavelength as a function of the horizontal angle of incidence (θ_H) as in Fig. 6(c) except with the $m-1$ and $m+1$ orders shifted by −12 nm and +12 nm respectively. The theoretical wavelength, given by Eq. (11), is in good agreement with the measured wavelength except at smaller angles of incidence where the shifted experimental results are slightly larger than that predicted by theory. In the case of varying the horizontal angle of incidence (θ_H) it is seen in Fig. 10(b) that the change due to path length is much more significant than the change due to refractive index.

Optics EXPRESS

In the experiment, wavelength tuning was limited by the FSR of the crystal. Substituting Eqs. (5) and (6) into Eq. (4) gives

$$\Delta\lambda_{\mathrm{FSR}} = \frac{\lambda_m^2}{\Delta nL} = \frac{\lambda_m^2 \cos\theta'_H \cos\theta'_V}{\Delta n_{bc} L_0 \sin\gamma_1 \sin\gamma_2}. \tag{12}$$

This equation describes the crystal FSR for a general beam path. Using the experimentally measured FSR, L_0 can be determined for crystal 1 and 2. For $\Delta n_{bc} = 0.0074$, $\theta_H = \theta_B$ and $\theta_V = 8°$ (dual wavelength region) with $\lambda_m = 764$ nm: $L_0 = 7.6$ mm for crystal 1 and $L_0 = 7.0$ mm for crystal 2. These values are in good agreement with the nominal value of $L_0 = 6.9$ mm when accounting for tolerance of the cut of the crystal and the spectrometer resolution.

The FSR is relatively unaffected by the beam path but inversely proportional to the crystal length, therefore wider wavelength tuning can be achieved with a shorter crystal. It is worth noting that a 10 mm long, Alexandrite plane-plane cylindrical rod was also used to try and obtain wavelength tuning, however it was not possible. This result suggest that the Brewster-cut of the gain medium is essential in providing polarisation induced losses for the wavelength selection.

4.2. *Temperature tuning: comparing model with experiment*

The theoretical model also enables some insight into the material properties of Alexandrite. The temperature tuning result can be used to determine the temperature dependence of the refractive index. Taking the derivative of Eq. (7) with respect to temperature gives

$$\frac{d\lambda_m}{dT} = \frac{\Delta n_{bc} \sin\gamma_1 \sin\gamma_2}{m} \frac{dL}{dT} + \frac{L}{m} \frac{d}{dT} \left(\Delta n_{bc} \sin\gamma_1 \sin\gamma_2\right). \tag{13}$$

Near Brewster angle incidence ($\theta_V = 0°$ and $\theta_H = \theta_B$): $\Delta n_{bc} \sin\gamma_1 \sin\gamma_2 \approx n_b - n_a = \Delta n_{ba}$. Assuming the rate of change of crystal length with temperature (dL/dT) is negligible, substituting for m using Eq. (7) and rearranging gives

$$\frac{d\Delta n_{ba}}{dT} = \frac{\Delta n_{ba}}{\lambda_m} \frac{d\lambda_m}{dT}. \tag{14}$$

Using $\Delta n_{ba} = 0.0055$, then for $d\lambda_m/dT = -0.07\,\mathrm{nm\,K^{-1}}$ and $\lambda_m = 750$ nm

$$\frac{d\Delta n_{ba}}{dT} = \frac{dn_b}{dT} - \frac{dn_a}{dT} = -0.5 \times 10^{-6}\,\mathrm{K^{-1}}. \tag{15}$$

This is in qualitative agreement with the previously measured value and its sign of $-1.1 \times 10^{-6}\,\mathrm{K^{-1}}$ at 1150 nm [38]. The experimental results of a decrease in wavelength with increasing temperature (Fig. 8) are also consistent with previous results [10] over 10-60 °C. In contrast, the thermo-optic dispersion results in [39] give a value of $+1.0 \times 10^{-6}\,\mathrm{K^{-1}}$ at $\lambda = 750$ nm. Although the photo-elastic effect has not been taken into account, its effect to the difference in the temperature dependence of the refractive indices is negligible. Further work may therefore be required into gaining a more thorough understanding of the temperature dependence of the refractive indices of Alexandrite, in particular for comparing the differences under lasing and non-lasing conditions.

5. Conclusion

This work has presented a wavelength tunable, dual wavelength and SQS red-diode-pumped Alexandrite laser formed of a plane-plane cavity and a Brewster-cut Alexandrite crystal. Tuning between 750 nm and 764 nm with a linewidth of ~ 15 GHz was obtained by tilting the crystal inside the cavity. Temperature tuning provided finer wavelength tuning at a rate of $-0.07\,\mathrm{nm\,K^{-1}}$. A stable dual wavelength emission was also obtained with a peak-to-peak separation of the FSR

Optics EXPRESS

of the crystal. Using a second crystal from a different supplier broader tuning of 747-768 nm and dual wavelength operation was obtained.

Stable SQS was measured over a narrow region of tuning with a minimum pulse duration of 660 ns at 135 kHz demonstrated. This result gives potential for Alexandrite to be used as an ultra-compact high repetition rate Q-switched source. The direct cause of the loss modulation is however unknown, but we believe to be related to the "population lens" effect that has been observed in other Cr-doped gain media. Verification of this effect and the optimisation and power scaling of the SQS cavity are interesting topics for future research.

The theoretical model is found to be in good agreement with the wavelength tuning results and dual wavelength separation. The wavelength tuning and dual wavelength operation reported in this work are not limited to Alexandrite and can be applied to other birefringent gain media. The theoretical model is general for any biaxial material and only needs small adaptation for uniaxial material. The analytical expressions can then be used to determine the wavelength and free spectral range given the material properties, in particular with shorter crystal length giving a wider tuning range.

Funding

Engineering and Physical Sciences Research Council (EPSRC) (EP/R00420X/1); Innovate Uk (132531).

References

1. M. Damzen, G. Thomas, A. Teppitaksak, E. Arbabzadah, W. Kerridge-Johns, and A. Minassian, "Diode-pumped alexandrite laser - a new prospect for remote sensing," in *2015 11th Conference on Lasers and Electro-Optics Pacific Rim (CLEO-PR),* vol. 1 (2015), pp. 1–2.
2. S. Burd, D. Leibfried, A. C. Wilson, and D. J. Wineland, "Optically pumped semiconductor lasers for atomic and molecular physics," Proc.SPIE **9349**, 93490 (2015).
3. C. Lefort, "A review of biomedical multiphoton microscopy and its laser sources," J. Phys. D: Appl. Phys. **50**, 423001 (2017).
4. M. Tani, P. Gu, M. Hyodo, K. Sakai, and T. Hidaka, "Generation of coherent terahertz radiation by photomixing of dual-mode lasers," Opt. Quantum Electron. **32**, 503–520 (2000).
5. C. Chow, C. Wong, and H. Tsang, "All-optical nrz to rz format and wavelength converter by dual-wavelength injection locking," Opt. Commun. **209**, 329 – 334 (2002).
6. J. Walling, O. Peterson, H. Jenssen, R. Morris, and E. O'Dell, "Tunable Alexandrite lasers," IEEE J. Quantum Electron. **16**, 1302–1315 (1980).
7. J. W. Kuper, T. Chin, and H. E. Aschoff, "Extended tuning range of alexandrite at elevated temperatures," in *Advanced Solid State Lasers,* (Optical Society of America, 1990), p. CL3.
8. E. Beyatli, I. Baali, B. Sumpf, G. Erbert, A. Leitenstorfer, A. Sennaroglu, and U. Demirbas, "Tapered diode-pumped continuous-wave alexandrite laser," J. Opt. Soc. Am. B **30**, 3184–3192 (2013).
9. A. Teppitaksak, A. Minassian, G. M. Thomas, and M. J. Damzen, "High efficiency >26 w diode end-pumped alexandrite laser," Opt. Express **22**, 16386–16392 (2014).
10. I. Yorulmaz, E. Beyatli, A. Kurt, A. Sennaroglu, and U. Demirbas, "Efficient and low-threshold alexandrite laser pumped by a single-mode diode," Opt. Mater. Express **4**, 776–789 (2014).
11. W. R. Kerridge-Johns and M. J. Damzen, "Temperature effects on tunable cw alexandrite lasers under diode end-pumping," Opt. Express **26**, 7771–7785 (2018).
12. M. J. Damzen, G. M. Thomas, and A. Minassian, "Diode-side-pumped alexandrite slab lasers," Opt. Express **25**, 11622–11636 (2017).
13. G. M. Thomas, A. Minassian, and M. J. Damzen, "Optical vortex generation from a diode-pumped alexandrite laser," Laser Phys. Lett. **15**, 045804 (2018).
14. G. M. Thomas, A. Minassian, X. Sheng, and M. J. Damzen, "Diode-pumped alexandrite lasers in q-switched and cavity-dumped q-switched operation," Opt. Express **24**, 27212–27224 (2016).
15. U. Parali, X. Sheng, A. Minassian, G. Tawy, J. Sathian, G. M. Thomas, and M. J. Damzen, "Diode-pumped alexandrite laser with passive sesam q-switching and wavelength tunability," Opt. Commun. **410**, 970 – 976 (2018).
16. A. Munk, B. Jungbluth, M. Strotkamp, H.-D. Hoffmann, R. Poprawe, J. Höffner, and F.-J. Lübken, "Diode-pumped alexandrite ring laser in single-longitudinal mode operation for atmospheric lidar measurements," Opt. Express **26**, 14928–14935 (2018).
17. A. Munk, M. Strotkamp, M. Walochnik, B. Jungbluth, M. Traub, H.-D. Hoffmann, R. Poprawe, J. Höffner, and F.-J. Lübken, "Diode-pumped q-switched alexandrite laser in single longitudinal mode operation with watt-level output power," Opt. Lett. **43**, 5492–5495 (2018).

Optics EXPRESS

18. X. Sheng, G. Tawy, J. Sathian, A. Minassian, and M. J. Damzen, "Unidirectional single-frequency operation of a continuous-wave alexandrite ring laser with wavelength tunability," Opt. Express **26**, 31129–31136 (2018).
19. W. R. Kerridge-Johns and M. J. Damzen, "Analytical model of tunable alexandrite lasing under diode end-pumping with experimental comparison," J. Opt. Soc. Am. B **33**, 2525–2534 (2016).
20. S. Ghanbari and A. Major, "High power continuous-wave dual-wavelength alexandrite laser," Laser Phys. Lett. **14**, 105001 (2017).
21. S. Manjooran, P. Loiko, and A. Major, "A discretely tunable dual-wavelength multi-watt yb:calgo laser," Appl. Phys. B **124**, 13 (2017).
22. T. Waritanant and A. Major, "Dual-wavelength operation of a diode-pumped nd:yvo4 laser at the 1064.1 & 1073.1nm and 1064.1 & 1085.3nm wavelength pairs," Appl. Phys. B **124**, 87 (2018).
23. E. Beyatli and U. Demirbas, "Widely tunable dual-wavelength operation of tm:ylf, tm:luag, and tm:yag lasers using off-surface optic axis birefringent filters," Appl. Opt. **57**, 6679–6686 (2018).
24. U. Demirbas, "Optimized birefringent filter design for broadly tunable multicolor laser operation of nd-based lasers: Nd:yag example," J. Opt. Soc. Am. B **35**, 2994–3003 (2018).
25. E. A. Arbabzadah and M. J. Damzen, "Fibre-coupled red diode-pumped alexandrite TEM00 laser with single and double-pass end-pumping," Laser Phys. Lett. **13**, 065002 (2016).
26. P. Loiko and A. Major, "Dispersive properties of alexandrite and beryllium hexaaluminate crystals," Opt. Mater. Express **6**, 2177–2183 (2016).
27. M. Born and E. Wolf, *Principles of Optics* (Pergamon Press, 1980, VI ed.).
28. S. T. Lai and M. L. Shand, "High efficiency cw laser-pumped tunable alexandrite laser," J. Appl. Phys. **54**, 5642–5644 (1983).
29. W. Gadomski and B. Ratajska-Gadomska, "Self-pulsations in phonon-assisted lasers," J. Opt. Soc. Am. B **15**, 2681–2688 (1998).
30. J. W. Kuper and D. C. Brown, "High-efficiency cw green-pumped alexandrite lasers," Proc.SPIE **6100**, 61000T (2006).
31. S. Ghanbari, R. Akbari, and A. Major, "Femtosecond kerr-lens mode-locked alexandrite laser," Opt. Express **24**, 14836–14840 (2016).
32. S. Ghanbari, K. A. Fedorova, A. B. Krysa, E. U. Rafailov, and A. Major, "Femtosecond alexandrite laser passively mode-locked by an inp/ingap quantum-dot saturable absorber," Opt. Lett. **43**, 232–234 (2018).
33. C. Cihan, A. Muti, I. Baylam, A. Kocabas, U. Demirbas, and A. Sennaroglu, "70 femtosecond kerr-lens mode-locked multipass-cavity alexandrite laser," Opt. Lett. **43**, 1315–1318 (2018).
34. C. Cihan, C. Kocabas, U. Demirbas, and A. Sennaroglu, "Graphene mode-locked femtosecond alexandrite laser," Opt. Lett. **43**, 3969–3972 (2018).
35. D. Skrabelj, I. Drevensek-Olenik, and M. Marincek, "Influence of the population lens on the em field evolution in chromium-doped laser materials," IEEE J. Quantum Electron. **46**, 361–367 (2010).
36. E. Beyatli, A. Sennaroglu, and U. Demirbas, "Self-q-switched cr:licaf laser," J. Opt. Soc. Am. B **30**, 914–921 (2013).
37. R. C. Powell and S. A. Payne, "Dispersion effects in four-wave mixing measurements of ions in solids," Opt. Lett. **15**, 1233–1235 (1990).
38. J. Walling, D. Heller, H. Samelson, D. Harter, J. Pete, and R. Morris, "Tunable alexandrite lasers: Development and performance," IEEE J. Quantum Electron. **21**, 1568–1581 (1985).
39. P. Loiko, S. Ghanbari, V. Matrosov, K. Yumashev, and A. Major, "Dispersion and anisotropy of thermo-optical properties of alexandrite laser crystal," Opt. Mater. Express **8**, 3000–3006 (2018).

155.198.12.188 {ts '2019-06-17 08:48:58'}